

Mechanism of $O(^3P)$ Formation from a Hydroxyl Radical Pair in Aqueous Solution

Edelsys Codorniu-Hernández,[†] Kyle Wm. Hall,^{†,‡} A. Daniel Boese,^{§,||} Daniel Ziemianowicz,[†] Sheelagh Carpendale,[‡] and Peter G. Kusalik^{*,†}

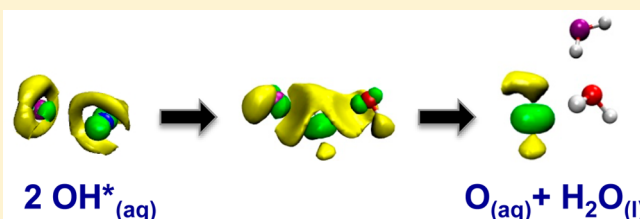
[†]Department of Chemistry, [‡]Department of Computer Science, University of Calgary, 2500 University Drive North West, Calgary, Alberta T2N 1N4, Canada

[§]Department of Chemistry, Physical and Theoretical Chemistry, University of Graz, Heinrichstraße 28/IV, 8010 Graz, Austria

^{||}Department of Chemistry, University of Potsdam, Karl-Liebknecht-Straße 24-25, 14476 Potsdam, Germany

S Supporting Information

ABSTRACT: The reaction mechanism for the rapid formation of a triplet oxygen atom, $O(^3P)$, from a pair of triplet-state hydroxyl radicals in liquid water is explored utilizing extensive Car–Parrinello MD simulations and advanced visualization techniques. The local solvation structures, the evolution of atomic charges, atomic separations, spin densities, electron localization functions, and frontier molecular orbitals, as well as free energy profiles, evidence that the reaction proceeds through a hybrid (hydrogen atom transfer and electron–proton transfer) and hemibond-assisted reaction mechanism. A benchmarking study utilizing high-level *ab initio* calculations to examine the interactions of a hydroxyl radical pair in the gas phase and the influence of a hemibonded water is also provided. The results presented here should serve as a foundation for further experimental and theoretical studies aimed at better understanding the role and potential applications of the triplet oxygen atom as a potent reactive oxygen species.



INTRODUCTION

Reactions involving radical systems in water are crucial in understanding many biochemical, atmospheric, and nuclear reactions.¹ It has been suggested that water molecules play a pivotal role in catalyzing radical reactions in solution.^{1–3} The pre- and postreactive complexes formed by weak interactions (e.g., hydrogen bonds, charge-transfer complexes) with water molecules can determine the course of both closed and open shell chemical reactions.^{2–4} Recently, a particular interaction that only radicals can form, the hemibonding or two-center three-electron interaction (also 2c–3e bonding), has attracted considerable attention.^{4–10} These interactions were initially described in 1931 by Pauling in one of his classic papers⁶ on the nature of the chemical bond and later in his book⁷ and have recently attracted attention in many different areas, such as free-radical chemistry in solution,^{5,11–16} solid¹⁷ and gas phases,^{5,18–21} organic and biochemical reactions,^{5,22–24} radiation studies,^{5,25–28} enzymology, and many others.

The hemibonding interaction has been extensively explored theoretically by Gill and Radom^{5,34} and by several subsequent studies about cationic radical complexes.^{35,36} In contrast to the complexes formed between closed shell systems, this incipient chemical bond,^{5,34} with a bond order of one-half, can determine the reaction channel that a system follows.⁵ Hemibonds are important because they can stabilize reaction intermediates during electron transfer processes, for example, in biological environments.⁵

An extensive review of the hemibonding interaction has been reported by Fourré and Silvi in 2007.⁵ Within the valence-bond formalism, the resulting resonance between the two Lewis structures obtained from the formation of the hemibond, which are mutually related by charge transfer, provides stability to this electronic arrangement. From the molecular orbital theory point of view, a closed shell orbital, typically a lone pair of one fragment, interacts with the singly occupied MO of a second fragment, resulting in a doubly occupied bonding MO (usually a σ orbital) and a singly occupied antibonding MO (σ^*) of the resulting molecule. The interacting MOs of the fragments should be close in energy; therefore, the strongest hemibonds should form when the two interacting fragments are chemically identical.

Over the past few years, we have published several studies^{9,37–40} focused on understanding the behavior of the hydroxyl radical (OH^\bullet) in aqueous environments. OH^\bullet is one of the most important recycling molecules in the Earth's atmosphere, being called the atmospheric vacuum cleaner.⁴¹ OH^\bullet is the main oxidizing constituent of the troposphere and causes the transformation of many trace components into water-soluble forms that can rain out and be removed from the troposphere. Correspondingly, the atmospheric concentration of OH^\bullet is very low, and its determination represents a

Received: June 4, 2015

significant analytical challenge. A different scenario arises when considering the reactivity of OH^\bullet *in vivo*. Although OH^\bullet is produced as part of our immune response to counteract/attack viruses or bacteria, its overproduction has been documented *in vivo* under conditions such as hypoxia, ischemia, and oxidative stress and has been directly related to fatal diseases such as cancer.^{42–48} OH^\bullet is a third-generation species of radicals that is derived from hydrogen peroxide (H_2O_2), which, in turn, is derived from the superoxide radical through the action of the enzyme superoxide dismutase.⁴⁴ Different reactive oxygen species are formed in measurable quantities in cells as a result of regular metabolism, for example, yielding 3×10^9 molecules of H_2O_2 per cell per hour.⁴⁹ H_2O_2 , in turn, readily decomposes⁴ to form OH^\bullet , although our bodies cannot eliminate OH^\bullet radicals by enzymatic reactions; rather, it relies on an external source of antioxidants for its elimination.^{45–47}

The past decade has witnessed some controversy around the existence of a $\text{OH}^\bullet\text{--OH}_2$ hemibonding interaction.^{8,9,37–40,50–53} While a hemibonded OH^\bullet species was used to assign experimental lines for OH^\bullet in water,^{8,50} other studies flagged such structures as an artifact of DFT functionals.⁵¹ A more recent extensive benchmarking study,⁹ comparing the results obtained with the HCTH/120 DFT functional with high-level *ab initio* methods, including corrections beyond the CCSD(T) level, has shown that the hemibond is, indeed, an alternative structure for OH^\bullet when the formation of H-bonds is impeded. These results are in full agreement with the recent work of Chipman^{8,50} and with the fact that the $\text{OH}^\bullet\text{--OH}_2$ hemibonds have been utilized to assign some experimental UV bands of OH^\bullet in solution.^{50,54,55} There is now ample evidence that high-level *ab initio* methods predict the existence of this interaction for several radical-molecular systems,⁵ with DFT functionals tending to overestimate slightly the stability of the hemibonded interactions.^{8,9}

Knowledge of OH^\bullet 's behavior when its local concentration increases, as can occur *in vivo*, may be very useful in its control. In a very recent paper,⁴⁰ we reported the formation of hydrogen peroxide when two OH^\bullet radicals encounter each other in solution in the singlet state, as expected, and observed production of a much more potent oxidant species, the triplet $\text{O}(\text{aq})$ or $\text{O}({}^3\text{P})$, when the two OH^\bullet encounter with a triplet-state electronic configuration. The formation of $\text{O}({}^3\text{P})$ has been previously studied theoretically^{56–59} and experimentally^{60–63} in the gas phase. Additionally, oxygen atoms had been previously suggested to be a primary species in irradiated water,^{63,64} an environment also favorable for OH^\bullet encounters, as well as the precursors of O_2 generated in γ -ray irradiated $\text{FeSO}_4\text{--CuSO}_4$ solutions.⁶⁵

In this article, we present details on the reaction mechanism for the formation of a triplet oxygen atom from two OH^\bullet radicals in the liquid phase, $2\text{OH}^\bullet(\text{aq}) \rightarrow \text{O}({}^3\text{P})(\text{aq}) + \text{H}_2\text{O}(\text{l})$, where we demonstrate that the reaction proceeds through the formation of a hemibonded OH^\bullet as a weakly bound prereactive complex. In the **Methods** section of this article, we provide details of the Car–Parrinello MD simulations that we have used to investigate the reaction, the DFT and *ab initio* calculations in the gas phase, and the visualization techniques utilized for displaying structural and electronic details. In the **Results and Discussion**, the local solvation structure of the two OH^\bullet radicals during the reaction is described, and we provide evidence of the hybrid and hemibond-assisted nature for the reaction mechanism. The evolution of electronic features during the reaction (i.e., spin densities, electronic localization

functions, frontier molecular orbitals) and free energy profiles are reported, as are benchmark results for the HCTH/120 DFT functional. The final section provides our conclusions.

METHODS

CPMD Simulations. Car–Parrinello⁶⁶ DFT-based molecular dynamics simulations (four independent trajectories) were performed with the CPMD⁶⁷ code to study $62\cdot\text{H}_2\text{O}\text{--}2\text{OH}^\bullet$ systems at 310 K in a cubic and periodic simulation box with a length of 12.56 Å. The local spin density approximation (LSDA) was used to account for the unpaired electrons on the OH^\bullet radicals. The HCTH/120⁶⁸ density functional was employed, and the valence–core interactions were described by Troullier–Martins⁶⁹ norm-conserving pseudopotentials. The valence electronic wave function was described with a plane wave basis with an energy cutoff of 90 Ry (120 Ry being utilized to obtain the electronic data). Fictitious electronic masses of 100 and 400 au were both employed. The fictitious electron kinetic energy and the dynamics of atoms were each controlled by a chain of three Nosé–Hoover thermostats⁷⁰ operating at characteristic frequencies of 6000 and 2000 cm^{-1} , respectively. During the equilibration and production runs, the total energy was monitored, as was the kinetic energy of the fictitious electronic degrees of freedom. The average fictitious kinetic energy was maintained at levels of 0.03 Ha and remained stable during the whole simulation. The time step was set to 0.1 fs. In previous reports,^{9,37–40} we characterized the solvation and mobility of OH^\bullet in water and ice, utilizing Car–Parrinello MD simulations with the same methodology described herein, including comparisons with the BLYP DFT functional.

Additional CPMD simulations of a system containing two OH^\bullet radicals in bulk ice were performed to help confirm the proposed reaction mechanism, as shall be explained in the **Results and Discussion**. For these simulations, an orthorhombic hexagonal ice system of 62 water molecules and two OH^\bullet radicals, with dimensions of 9.0, 15.6, and 14.7 Å, was used. This block of ice was generated using crystallographic positions for oxygen atoms and ice rules for assignment of the hydrogen atom positions.⁷¹ One of the OH^\bullet radicals was placed in an in-lattice position by removing a hydrogen atom from one water molecule, whereas the second OH^\bullet was added to the center of the same ice cage. Both of these positions of the radicals have been detected experimentally^{72–74} and theoretically.³⁹ The simulation strategy was similar to the one applied for the aqueous system, with the key difference being a simulation temperature of 190 K for the ice system.

Benchmark Study. Previous work^{37,39} for OH^\bullet aqueous systems has demonstrated that HCTH/120 within CPMD provides superior results to those of BLYP, where the latter functional tends to predict an overstructured system. A more recent benchmark study⁹ compared the HCTH/120 functional with high-level (MP2, basis set limit CCSD(T) and beyond) *ab initio* calculations to characterize accurately the hemibonded interaction and its energy relative to well-defined hydrogen-bond interactions.⁹ This gas-phase *ab initio* study validated the HCTH/120 functional for its ability to reasonably describe the possible interactions of OH^\bullet in an aqueous environment.⁹ In this article, we provide a benchmark study of the HCTH/120 DFT functional with high-level *ab initio* calculations in predicting the interactions of two OH^\bullet radicals in the gas phase, as well as the effect of including a hemibonded water in the system. $\text{OH}^\bullet\text{--OH}^\bullet$ interactions have been studied in the

gas phase with full optimization of the system at every constrained $\text{O}^\bullet\text{--O}^\bullet$ distance; unlike previous gas phase calculations,⁸ we did not impose additional constraints, allowing the system to explore all possible configurations for each constrained distance. Post-Hartree–Fock gas-phase calculations utilizing coupled-cluster levels up to single, double, and perturbative triple excitations (CCSD(T)) were applied in combination with Dunning's aug-cc-pVnZ correlation consistent basis sets (going from triple- ζ to quadruple- ζ quality). The HCTH/120⁶⁸ DFT functional was tested, utilizing the same basis sets. For the CCSD(T) geometry optimizations utilizing a UHF reference function, we employed the CFOUR program,⁷⁵ whereas for the rest of the computations, we used MOLPRO.⁷⁶ Due to previous suggestions of multireference character in this system,⁵⁷ multistate (MS)-CASPT2 and MS-MRCISD calculations were also performed. The optimizations at the MS-CASPT2 level were done with a complete active space (CAS) using 12 electrons in 10 orbitals together with the 6-311+G(3df,2pd) basis set with no symmetry and using 10 electrons in 10 orbitals with the same basis set for the calculations including a water molecule. In the former case, the four lowest states were optimized in the multistate treatment. Extending the active space or varying the number of optimized states did not change the results. In addition to the geometries optimized by this method, we performed MS-MRCISD+D calculations employing the same CAS and the same multistate treatment as well as ROHF-CCSD(T) single points together with the aug-cc-pVTZ basis set. When going from the 6-311+G(3df,2pd) to the aug-cc-pVTZ basis set, the results remained unchanged. For the Davidson corrections ("D"), we used rotated cluster corrections with a rotated reference energy. Finally, we determined UHF-CCSD(T)/aug-cc-pVQZ single-point energies on the UHF-CCSD(T)/aug-cc-pVTZ geometries with no change in the results.

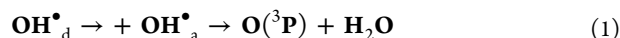
Constrained MD (CMD). CMD simulations⁷⁷ were utilized to determine free energy profiles for the formation of $\text{O}(\text{aq})$. Two different CMD simulations were performed: one utilizing a $\text{O}^\bullet\text{--H}^\bullet$ separation, where O^\bullet and H^\bullet are the oxygen atom that receives the hydrogen atom transfer during the reaction and the hydrogen atom that is transferred, respectively. The second CMD simulation also includes a restriction to impede the formation of hemibonds between water molecules and the OH^\bullet that donates the hydrogen atom in the reaction. For this second constraint, the coordination number of the water oxygens within 2.6 Å of the oxygen atom that donates the hydrogen atom during the reaction was required to be zero. For each 0.1 Å increment, the average constraint force was measured over a 20 ps trajectory. From such simulations, the free energy profile was obtained from a straightforward thermodynamic integration over the chosen coordinate.

Video Visualization Methods. The videos in Supporting Information were generated using an in-house Processing program; Processing is available at <https://processing.org/>. In the videos, the two OH^\bullet radicals were rendered completely opaque, and the surrounding atoms were rendered with increasing transparency the farther they were from the two OH^\bullet radicals. The electronic surfaces are the result of interpolating the voxel data provided by CPMD and rendering a small, semitransparent sphere at interpolation points whose position was within 2.0 Å of either hydroxyl radical's oxygen atom and whose value was within the range of interest for a given electronic property. This range corresponded to 3.75×10^{-4} to 4.25×10^{-4} for the positive spin density (yellow

surface) and -0.0335 to -0.0265 for the negative spin density (green surface). For the video of the evolution of the electronic localization functions, this range corresponds to 0.85 to 0.87 for both the alpha (cyan) and beta (pink) surfaces. In the case of the video showing the evolution of the molecular frontier orbitals (HOMO and HOMO $- 1$) during the reaction, this range corresponds to -0.031 to -0.029 and 0.039 to 0.041 for the negative and positive lobes, respectively. Furthermore, for this video, the red, blue, purple, and green surfaces correspond to the negative lobe of the HOMO, the positive lobe of the HOMO, the negative lobe of the HOMO $- 1$, and the positive lobe of the HOMO $- 1$, respectively. In the videos, the tails behind the atoms indicate the recent positions of the atoms in the local frame of reference of the videos. Detailed information about how these videos were created can be found in previous work.^{40,78}

RESULTS AND DISCUSSION

Local Solvation Structure of the OH^\bullet Radicals. An understanding of the local solvation structure of the two hydrated OH^\bullet radicals before and during the reaction is crucial in the description of the reaction mechanism that yields an $\text{O}(\text{aq})$ in water. Previous extensive Car–Parrinello MD simulations have elucidated the solvation of a single OH^\bullet in water,³⁷ in agreement with other reports.⁷⁹ In this previous report,³⁷ the OH^\bullet was found to exist in an inactive state, $\text{OH}^\bullet(\text{H}_2\text{O})_4$, in which OH^\bullet interacts with three H-bond-donating neighbors and one H-bond-accepting neighbor.³⁷ In the discussion of the solvation of the two OH^\bullet radicals involved in the disproportionation reaction and its influence on the reaction mechanism, the following nomenclature will be used



where $\text{OH}^\bullet_{\text{d}}$ is the OH^\bullet donor of a hydrogen atom in the reaction converting to $\text{O}(\text{aq})$ and $\text{OH}^\bullet_{\text{a}}$ is the acceptor of the hydrogen atom becoming a water molecule. Henceforth, the oxygen atoms of $\text{OH}^\bullet_{\text{d}}$ and $\text{OH}^\bullet_{\text{a}}$ are represented in figures by blue and purple spheres, respectively.

A representation of the initial configuration observed during the simulations of the OH^\bullet pair in water is shown in Figure 1(I), where the two OH^\bullet radicals are found to have a local solvation structure that resembles the inactive OH^\bullet in aqueous solution. For the OH^\bullet pair, one of the H-bond-donating waters of the inactive $\text{OH}^\bullet(\text{H}_2\text{O})_4$ is substituted by the other OH^\bullet , yielding the structure $(\text{H}_2\text{O})_3\text{--HO}^\bullet\text{--OH}^\bullet(\text{H}_2\text{O})_3$. In our previous report,³⁷ it was found that the OH^\bullet needs to experience the appropriate structural fluctuations to escape from the inactive state to allow it to engage in H-transfer with one of its neighboring water molecules. In its active state, the OH^\bullet has a $\text{OH}^\bullet(\text{H}_2\text{O})_3$ arrangement, formed through the weakening of the $[\text{H}_2\text{O--HO}^\bullet]$ hydrogen bond (i.e., where $\text{OH}^\bullet_{\text{d}}$ donates a H-bond to a water molecule). As observed in Figure 1(II), both OH^\bullet radicals in the pair experience a weakening of this interaction, although a more dramatic change is observed for $\text{OH}^\bullet_{\text{d}}$. As we shall detail below, $\text{OH}^\bullet_{\text{d}}$ first experiences the weakening of this H-bond and then the same water molecule quickly forms a hemibonded interaction with the radical. With its weakened donor hydrogen bond, $\text{OH}^\bullet_{\text{a}}$ has become an active species ready to accept a H-transfer. The hemibonded $\text{OH}^\bullet_{\text{d}}$ immediately (within 77 fs) changes its orientation to donate a hydrogen bond to the active $\text{OH}^\bullet_{\text{a}}$ (Figure 1(III)). As the H-transfer proceeds (Figure 1(IV)) and

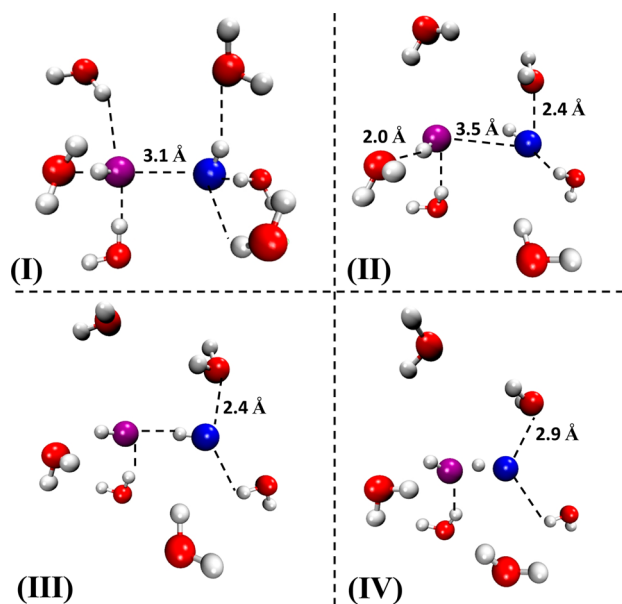


Figure 1. Snapshots representing the local solvation around the two OH• radicals (oxygen represented with purple and blue spheres) for different steps during the disproportionation reaction $2 \text{OH}^\bullet(\text{aq}) \rightarrow \text{O}(^3\text{P})(\text{aq}) + \text{H}_2\text{O}(\text{l})$ in the triplet state for a $62\text{-H}_2\text{O}-2\text{OH}^\bullet$ system at 310 K. Dashed lines represent key interactions within the system, where some important distances are provided. (I) The initial state showing a 4-fold OH•(X₄) coordination, where X corresponds to three water molecules (one H-bond acceptor and two H-bond donors) and the neighboring OH•; (II) the step in which the weakening of the [H₂O-HO•] hydrogen bond is observed for both OH• radicals, along with formation of a hemibonded interaction; (III) the step in which the hemibonded OH•_a adopts a head-to-tail orientation and donates a H-bond to OH•_b; (IV) the step in which the hydrogen atom is observed to be equidistant from the two OH• oxygens. The whole reaction, i.e., conversion from (I) to (IV), occurs in approximately 200 fs.

the O(³P) forms, the hemibond of the neighboring water evolves into a H-bond arrangement. It is interesting to see that this reaction, in which the OH• pair transforms into the biradical O(³P), has aspects similar to those observed for the H-transfer reaction between OH• and water.³⁷ A key difference lies in the fact that this reaction appears to be hemibond-assisted. In the next subsection, we will explore the influence of the hemibonded arrangement in the free energy profile of this reaction in water.

The repositioning of the water molecule that was accepting a OH• H-bond to a hemibonding arrangement is potentially the rate-limiting step for this reaction. The RAMT (radially angularly mapped trajectories) plots, used in our previous report⁴⁰ and discussed in detail in a forthcoming visualization paper, are a useful tool to track the temporal evolution of the local structure during the reaction, as can be seen in Figure 2. The behavior observed in Figure 2 is representative of the pattern seen in the four independent simulation trajectories (see details in Supporting Information). Focusing our attention on the A-side of the plot (corresponding to OH•_a), it is possible to follow the bold green line that represents the angle–distance evolution of the oxygen of a water molecule (yellow sphere in the inset structures) from point (I), in which the water molecule is accepting a H-bond from OH•_b, to point (II), in which the water hemibonds the OH•_b leaving the radical without a H-bond acceptor. This corresponds to the

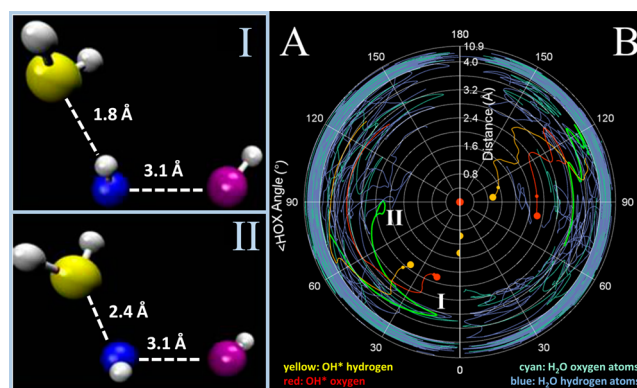


Figure 2. Local frame representation of a typical system trajectory where the $2\text{OH}^\bullet(\text{aq}) \rightarrow \text{O}(^3\text{P})(\text{aq}) + \text{H}_2\text{O}$ reaction occurs. Sides A and B correspond to the RAMT⁴⁰ plots for OH•_a and OH•_b, respectively. The two semicircular RAMT plots are divided by a white vertical line, where the final positions of the OH• atoms that define the frame of reference are shown as semicircles along the line. To understand the RAMT plot for a given OH•, imagine placing the radical's oxygen atom at the origin of the OH• frame of reference and aligning the O–H bond (the radical's C_∞ symmetry axis) with the zenith direction. Plotting atomic trajectories in this (r,θ)-space shows the time evolution of the system from the perspective of the radical. The large dots indicate the final positions of the atoms of the other OH• within the frame of reference of the central OH•. The radial distance scale has two linear regions (0.0 to 4.0 Å and 4.0 to 10.9 Å). The arrangement of the OH• pair and the water molecule (yellow sphere) that hemibonds the OH• is represented on the left side of the figure in frames I and II. These arrangements are also labeled on the trajectories shown in (A) and coincide with representations (I) and (II) shown in Figure 1.

change observed in Figure 1 between configurations (I) and (II).

In Figure 1(III), it is notable that OH•_a has also experienced a weakening of the [H₂O-HO•] hydrogen bond already observed in Figure 1(II). OH• is a very good H-bond donor; therefore, the rotation of OH•_b, taking the OH• radicals from a side-by-side orientation (Figure 1(II)) to a head-to-tail, orientation (Figure 1(III)), is expected.

The evolution of the atomic separations and charges of the same representative trajectory is presented in Figure 3, where the regions denoted with black dashed lines roughly correspond to the four main steps of the reaction represented in Figure 1. As shown in Figure 3a, the evolution of the separations of O•_a-H₁ and O•_a-H₂ intercept at about 200 fs, highlighted with a red dashed circle, and can be seen as the transition state (point at which the hydrogen atom is equidistant between the two oxygens). The separation between the oxygens of the two radicals exhibits a minimum approach at this transition state. The lines representing the evolution of the separation between OH•_a and its initially H-bond-accepting water neighbor confirms that during the reaction the hemibonding interaction between the water and OH•_a forms in step II, whereas it can be seen from Figure 3a that the weakening of the [H₂O_{w-A}-HO•_a] hydrogen bond begins in step II but continues during step III. It is important to note that the OH•_a-H₂O hemibonding interaction is observed only during the reaction and does not persist after formation of the O(³P) (see videos shown in Supporting Information). Additionally, the appearance of this hemibonded interaction is apparently not a system size effect, as was previously observed for smaller 31-H₂O-OH•

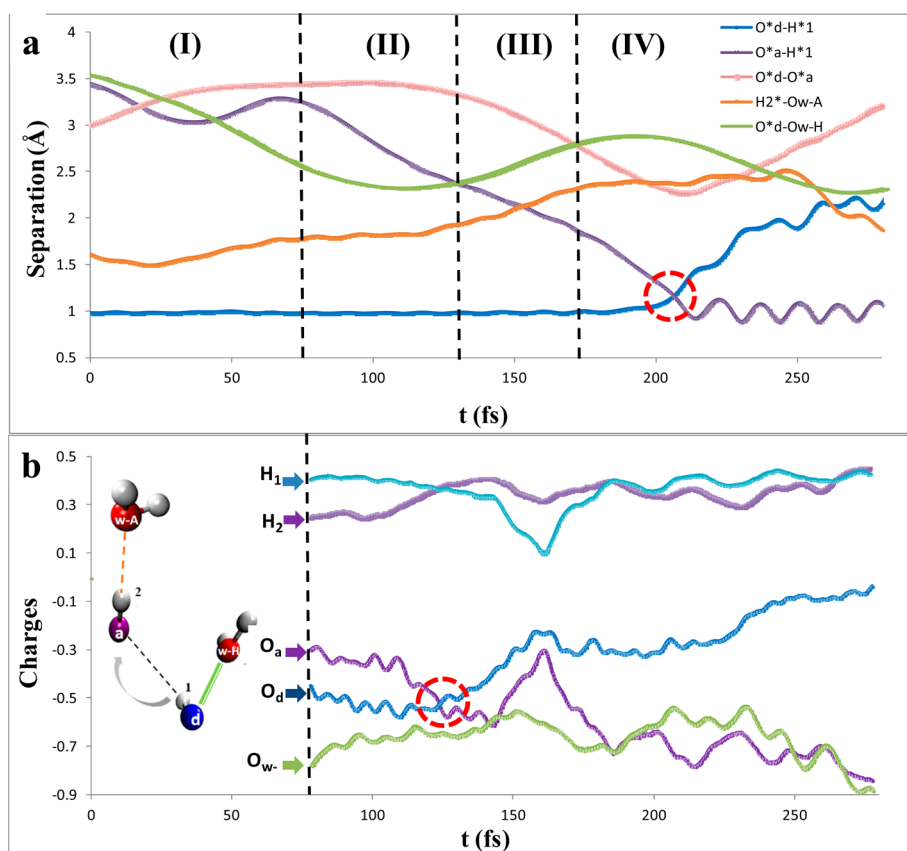


Figure 3. Evolution of (a) atomic separations and (b) atomic charges during 200 fs of a Car–Parrinello molecular dynamics simulation of a 62·H₂O–2OH[•] system at 310 K. The areas identified with Roman numerals correspond roughly to the configurations shown in Figure 1. In (a), the atomic separations of O[•]_d–O[•]_a, O[•]_a–H[•]₁, O[•]_d–H[•]₁, H[•]₂–O_w–A, and O[•]_d–O_w–H are represented by light pink, purple, blue, orange, and green solid lines, respectively. In (b), the charges of O[•]_d, O[•]_a, O_w–H, H[•]₁, and H[•]₂ are represented by dark blue, dark purple, green, blue, and purple solid lines, respectively. Atom labels for both figures are provided in the inset of (b). The colors orange and green utilized for the representation of H-bonds in the inset corresponds to the colors of the separations represented in (a).

systems,³⁷ since here the hemibond forms only transiently during the reaction.

Benchmarking of DFT Results in the Gas Phase. As stated in the [Introduction](#), the formation of hemibonds between OH[•] and water has been supported by both experimental and theoretical observations,^{8,50} where DFT functionals tend to slightly overestimate the strength of these interactions. To further validate the behavior observed here, a benchmark study has been performed, where the HCTH/120 functional is compared with CCSD(T) calculations. Since there was preliminary evidence from previous work⁵³ that single-reference methods may not correctly describe some open shell species at very short O[•]–O[•] separations on this potential energy surface, multistate-MRCISD+D and multistate-CASPT2 calculations have also been included (see details in the [Methods](#) section).

Figure 4 shows the potential energies obtained by various methods for the range of O[•]–O[•] separations explored by the system during the reaction to produce O(³P) in the aqueous phase, from 2.3 to 3.0 Å. From 2.3 to 2.6 Å, the OH[•]–OH[•] dimer configuration is obtained, whereas the H-bond configuration is obtained from 2.7 to 3.0 Å (see inset). It is important to state that for all of the methods the ground state of the system is O(³P) + H₂O (see details in the [Supporting Information](#)), in accord with the results obtained theoretically in the condensed phase⁴⁰ as well as in previous gas-phase calculations^{56–59} and experiments.^{60–63} Because we are

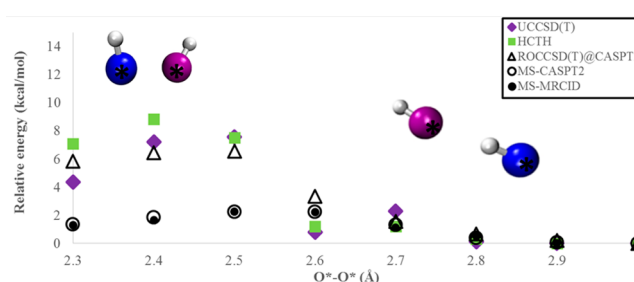


Figure 4. Relative energies (kcal/mol) for O[•]–O[•] separations from 2.3 to 3.0 Å utilizing different methods (see legend). Configurations from 2.3 to 2.6 Å correspond to the triplet-state HO[•]–OH[•] dimer, whereas those from 2.7 to 3.0 Å are H-bond configurations (see insets). Only the O[•]–O[•] separation has been constrained, allowing the system otherwise to explore different configurations at each separation. Energy values are relative to the H-bond configuration. Note that the symbols overlap for all of the methods for 2.9 and 3.0 Å.

interested only in bound states in this benchmarking study, all energies have been reported relative to the first local minimum, that is, the H-bond configuration.

It can be seen in Figure 4 that the various reference methods yield somewhat different results, especially for the dimer arrangements. Notably, UCCSD(T) and ROCCSD(T) differ at shorter separations, indicating some multireference character for these systems. This is emphasized further by the difference

between the multireference methods and CCSD(T) for short distances; HCTH is more reminiscent of both CCSD(T) curves. Whereas the multireference character of the OH dimer system at short distances has been reported previously⁵⁷ and MS-MRCISD and MS-CASPT2 agree well with each other, much more elaborate calculations, using, for example, MRCCSD(T), are part of future work that should provide additional insights into which method is actually the most accurate. Furthermore, we might assume that the radical character of OH• will be more shielded as additional water molecules are added to the system.

The above conjecture is confirmed by larger gas-phase calculations that include the OH•–OH• pair and a single water molecule hemibonded to OH•_d. As can be seen from Figure 5,

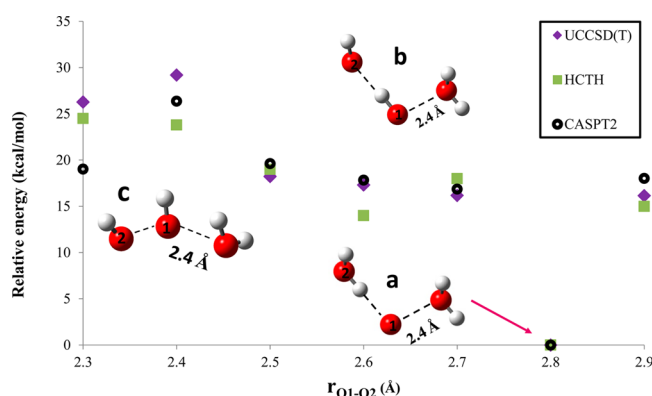


Figure 5. Relative energy (kcal/mol) as a function of the oxygen–oxygen separation (Å) for a gas-phase OH•–OH• pair in the triplet state when a water molecule is hemibonded to the hydrogen-atom-donating radical. In these calculations, the O₁–O distance was constrained at 2.4 Å for all points. UCCSD(T) (purple diamonds markers), CASPT2 (black circle markers), and the HCTH/120/aug-cc-pVQZ DFT functional (green squares markers) were utilized (see details in the Methods section). Three different configurations are observed and are shown in the insets, represented by “a” (at 2.8 Å), “b” (at 2.6, 2.7, and 2.9 Å), and “c” (2.0 to 2.5 Å). At 2.8 Å, both methods convert 2OH• + H₂O to O(³P) + 2H₂O during the optimization. Structure “a” corresponds to the minimum energy configuration for all utilized methods.

the results from the three methods, HCTH, UCCSD(T), and CASPT2, are in much better agreement over the full range of separations than those in Figure 4; the additional water molecule apparently results in the system having less multireference character. Together, the results from Figures 4 and 5 help to confirm the reliability of the present Car–Parrinello simulations of this aqueous system utilizing the HCTH functional, which finds a reasonably large free energy difference between the species O(³P) + H₂O and the HO•–OH• dimer and emphasizes the importance of the solvent effects, specifically a hemibonded water, in these systems.

As we have detailed in our previous gas-phase study,⁹ OH• has the ability to form hemibonds when the formation of hydrogen bonds is impeded (predicted by both HCTH and CCSD(T)), where, for small O•–O• separations, the DFT functional may tend to slightly overestimate the stability of hemibonds. However, as evidenced in Figure 4, multireference methods predict even smaller energies for the shorter O•–O• separations than those predicted by HCTH; a more extensive characterization of the HO•–•OH dimer (also known as triplet hydrogen peroxide) is currently in progress.

Hybrid and Hemibond-Assisted Reaction Mechanism.

On the basis of the above results, there is ample evidence from our four independent trajectories featuring the reaction in water, and supported by gas-phase calculations, that the reaction proceeds through a hemibond-assisted mechanism. In this section, a more detailed description of the reaction mechanism is provided. Figure 6 summarizes the evolution of the local structure, the electronic spin density, the electron localization function, and the molecular frontier orbitals (HOMO and HOMO – 1) during the reaction. Additionally, videos of the evolution of these electronic structure measures are provided in Supporting Information. As observed in column B of Figure 6, the spin density of the system is initially localized on the two OH•, becoming more delocalized across the two OH• and the water that approaches OH•_d to form a hemibond at about 80 fs. At about 120 fs, the spin density on OH•_d already begins to resemble that of an isolated oxygen atom, O(³P), while the hydrogen is still 1.5 Å from the OH• oxygen that accepts the transfer. The isosurfaces representing the evolution of the ELF show a similar behavior. At 120 fs, the ELF has evolved from one characteristic of a OH• to one that already resembles the O(³P). At 160 fs, when the hydrogen atom being transferred is not yet equidistant between the two oxygens, the ELF appears to have fully transitioned into one characteristic of an O(³P). For this system, the HOMO and HOMO – 1 are almost degenerate orbitals, and the HOMO appears to be consistently localized on OH•_d, whereas HOMO – 1 shows a more delocalized behavior that involves the hemibonded water as early as 80 fs.

The changes observed at about 120 fs, when the hydrogen-atom-donating oxygen is already exhibiting the electronic features of an isolated oxygen atom while the hydrogen atom being transferred is still closer to OH•_d, is consistent across all of the electronic structure measures examined. This tendency also agrees with the behavior apparent in the atomic separations and the evolution of the atomic charges (cf. Figure 3a,b). In Figure 3, a time lag is observed between the point at which the charges change for the two oxygen atoms involved in the reaction (see red dotted circle in Figure 3b) and the point at which the hydrogen atom being transferred is equidistant from the two OH• oxygens (see red dotted circle in Figure 3a). These features are indicative of a hybrid reaction mechanism,⁷³ apparently involving aspects of hydrogen atom transfer (HAT) and electron–proton transfer (EPT). In this hybrid mechanism, the electron transfer appears to precede the transfer of the hydrogen/proton. It is interesting to note that this behavior is similar to the hybrid mechanism observed for the H-transfer reaction from a water molecule to a OH• in aqueous environments.³⁸ The key difference here is that the intervention of a hemibonded water appears to be a necessary step for the reaction to take place. Detailed videos of the evolution of the spin density, HOMO and HOMO – 1, and electronic localization function during the reaction are provided in Supporting Information, where the complexity of the 62·H₂O–2OH• system has been reduced by focusing attention only on the molecules that are directly involved in the reaction.

To shed further light on the influence of the hemibonded interaction in this reaction mechanism, additional free energy calculations were performed, and the results are provided in Figure 7. Constrained MD simulations were utilized to generate free energy profiles for the reaction (see the Methods section) in which the O_a–H• distance, *r*, was constrained to values between 0.9 Å (i.e., in which the H-transfer is completed) and

Step	Time (fs)	A) Local structure	B) Spin density	C) ELF	D) HOMO	E) HOMO-1
I	0					
II	80					
	120					
III	160					
IV	190					
	6750					

Figure 6. Electronic features of selected configurations during the $2\text{OH}^{\bullet}(\text{aq}) \rightarrow \text{O}(^3\text{P})(\text{aq}) + \text{H}_2\text{O}(\text{l})$ reaction in the triplet state (see Figures 1 and 3 for a definition of the steps). Column A shows the relative orientations of the three species ($\text{OH}^{\bullet}_{\text{d}}$, $\text{OH}^{\bullet}_{\text{a}}$, and the hemibonded water) directly involved in the reaction, where the orientations of the configurations are preserved across a particular row (columns A–E). Column B provides the spin density distribution with yellow (value of +0.0004) and green (value of −0.03) isosurfaces. Column C presents the ELF- α as cyan isosurfaces (threshold 0.85) and the ELF- β as pink isosurfaces (threshold 0.85). Column D shows the evolution of the HOMO, where red and blue isosurfaces have values of −0.03 and +0.04, respectively. The same isovalues were employed for the HOMO − 1 isosurfaces represented in column E.

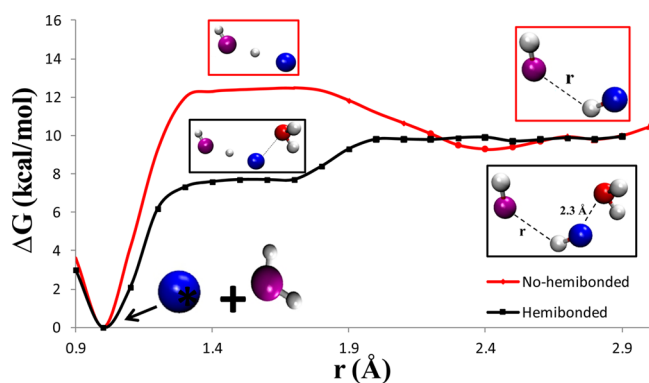


Figure 7. Free energy (ΔG) profiles at 310 K for the formation of $\text{O}(^3\text{P})$ from a triplet-state OH^{\bullet} pair within a $62\cdot\text{H}_2\text{O}-2\text{OH}^{\bullet}$ system utilizing constrained MD simulations. The black solid line shows the results obtained when the $\text{O}_{\text{a}}-\text{H}^{\bullet}$ distance, r , (defined in the inset) is utilized as a constraint, where H^{\bullet} is the hydrogen atom being transferred during the reaction. For the values represented by the red solid line, an additional constraint was employed to impede the formation of the $\text{H}_2\text{O}-\text{OH}^{\bullet}_{\text{d}}$ hemibond (see details in the Methods section). In each case, representative configurations, showing only the molecules directly involved, are provided as insets. In the determination of values for ΔG , contributions from the pV term were assumed to be negligible.

2.9 Å (corresponding to the OH^{\bullet} pair). Figure 7 includes results when a hemibonded water is present as well as when the formation of the hemibond between a water molecule and

$\text{OH}^{\bullet}_{\text{d}}$ has been impeded. The difference between these two curves confirms that the hemibonding interaction is an important step for hydrogen atom transfer. Specifically, when the hemibonded water is present, the free energy profile exhibits a barrier-free $2\text{OH}^{\bullet}(\text{aq}) \rightarrow \text{O}(^3\text{P})(\text{aq}) + \text{H}_2\text{O}(\text{l})$ reaction (i.e., going from right to left in Figure 7), whereas a barrier of about 2 kcal/mol is apparent when the formation of the $\text{H}_2\text{O}-\text{OH}^{\bullet}_{\text{d}}$ hemibond is impeded.

Additional confirmation of the role of the local structure and the importance of the hemibonded $\text{OH}^{\bullet}_{\text{d}}$ for the formation of $\text{O}(^3\text{P})$ from two OH^{\bullet} radicals in water was obtained from CPMD simulations of a system containing two OH^{\bullet} radicals in bulk ice, as described in the Methods section. In the liquid system, the reaction was observed to occur in 200 fs; in the ice system, no reaction was observed after 8 ps. Ice is a highly constrained system in which the formation of both the weakly bonded $\text{OH}^{\bullet}_{\text{d}}-\text{OH}_2$ complex and the active $\text{OH}^{\bullet}_{\text{a}}$ structure is impeded; both arrangements are apparently crucial steps for the reaction under study.

Taking into account all of the above observations, the reaction mechanism for $\text{O}(^3\text{P})$ production in aqueous solution from two OH^{\bullet} radicals in the triplet state involves the following set of key steps:

- (1) weakening of the $[\text{H}_2\text{O}-\text{HO}^{\bullet}_{\text{d}}]$ hydrogen bond through local structural fluctuations, with this water molecule then forming a transient hemibond with $\text{OH}^{\bullet}_{\text{d}}$;
- (2) formation of an active state transient $\text{OH}^{\bullet}_{\text{a}}(\text{H}_2\text{O})_2$ structure through the weakening of the $[\text{H}_2\text{O}-\text{HO}^{\bullet}_{\text{a}}]$ hydrogen bond;

- (3) formation of a $(\text{HO}_a\text{--HO}_d\text{--H}_2\text{O})^{\bullet\bullet}$ complex, with the two OH^\bullet radicals in a head-to-tail orientation and a water molecule hemibonded to OH^\bullet_d to facilitate an early electron transfer;
- (4) completion of the HAT/EPT reaction, resulting in a triplet $\text{O}(^3\text{P})$ and a new water molecule.

CONCLUSIONS

Extensive Car–Parrinello molecular dynamics simulations of two OH^\bullet radicals in liquid water (a $62\cdot\text{H}_2\text{O}\text{--}2\text{OH}^\bullet$ system) provide significant insights into the mechanism for formation of the triplet oxygen atom $\text{O}(^3\text{P})$, a much more potent biradical species, via the $2\text{OH}^\bullet(\text{aq}) \rightarrow \text{O}(^3\text{P})(\text{aq}) + \text{H}_2\text{O}(\text{l})$ reaction. Examination of the local solvation structure around the two OH^\bullet radicals from four independent MD trajectories reveals that both radicals are initially in a 4-fold coordination environment, $\text{OH}^\bullet(\text{X})_4$, resembling the inactive structure previously observed³⁷ for a OH^\bullet radical in water. The reaction generating $\text{O}(^3\text{P})$ appears to be a fast process, occurring within 200 fs, and exhibits a hybrid mechanism, with features of both hydrogen atom transfer and electron–proton transfer reactions. In this regard, the reaction mechanism resembles the one previously determined for the H-transfer between a water molecule and OH^\bullet in water, with the additional feature of a hemibond-assisted step leading to the formation of a $(\text{HO}^\bullet\text{--HO}^\bullet\text{--OH}_2)$ complex. The formation of hemibonds has been previously reported to play a role in assisting electron transfer reactions. Free energy profiles have confirmed that the reaction is a barrierless disproportionation reaction, although impeding the formation of the hemibond results in a reaction barrier of about 2 kcal/mol. A benchmark study demonstrates that a gas-phase triplet-state OH^\bullet pair has multireference character, particularly at shorter $\text{O}^\bullet\text{--O}^\bullet$ separations; HCTH and UCCSD(T) are in good agreement, particularly when a water molecule is included in the gas-phase calculation, confirming the reliability of the Car–Parrinello simulations utilizing the HCTH functional to describe the OH^\bullet pair in an aqueous environment.

Our findings have major implications on the scientific understanding of the potential impacts of high local OH^\bullet concentrations, such as within nuclear infrastructure and under certain circumstances *in vivo* such as under hypoxia, ischemia, and oxidative stress.^{42–48} In addition, the generation of $\text{O}(^3\text{P})$ aqueous soluble precursors, as a unique oxidant, is an active area of study.⁸⁰ Therefore, the details of the reaction mechanism for the production of $\text{O}(^3\text{P})$ provided here are both of fundamental importance and key to advancements across a wide range of fields.

ASSOCIATED CONTENT

Supporting Information

The Supporting Information is available free of charge on the ACS Publications website at DOI: 10.1021/acs.jctc.5b00783.

Radially angularly mapped trajectory (RAMT) plots from several other CPMD simulation trajectories; full list of authors for ref 1 (PDF).

Videos capturing the evolution of the electronic isosurfaces during the reaction (MPG, MPG, MPG).

AUTHOR INFORMATION

Corresponding Author

*E-mail: pkusalik@ucalgary.ca.

Funding

We are grateful for the financial support of the Natural Sciences and Engineering Research Council of Canada, the Alberta Innovates-Technology Futures, and the Canadian Foundation for Innovation. We also acknowledge computational resources made available via WestGrid (www.westgrid.ca) and the University of Calgary. K.-Wm.H. acknowledges funding from the Izaak Walton Killam Pre-Doctoral Scholarship Program and the Vanier CGS Program. S.C. acknowledges funding from GRAND, SurfNet, NSERC, AITF, SMART Technologies, and the University of Calgary.

Notes

The authors declare no competing financial interest.

ACKNOWLEDGMENTS

A.-D.B. would like to thank Prof. Peter Saalfrank (University of Potsdam) for providing computational time and useful discussions.

REFERENCES

- (1) Garrett, B. C.; et al. *Chem. Rev.* **2005**, *105*, 355–3900.
- (2) Otto, R.; Brox, J.; Trippel, S.; Stei, M.; Best, T.; Wester, R. *Nat. Chem.* **2012**, *4*, 534–538.
- (3) Tentscher, P. R.; Arey, J. S. *J. Chem. Theory Comput.* **2013**, *9*, 1568–1579.
- (4) Li, J.; Li, Y.; Guo, H. *J. Chem. Phys.* **2013**, *138*, 141102.
- (5) Fourré, I.; Silvi, B. *Heteroat. Chem.* **2007**, *18*, 135–160 and references therein..
- (6) Pauling, L. *J. Am. Chem. Soc.* **1931**, *53*, 3225.
- (7) Pauling, L. *The Nature of the Chemical Bond*; Cornell University Press: Ithaca, NY, 1948.
- (8) Chipman, D.-M. *J. Phys. Chem. A* **2011**, *115*, 1161.
- (9) Codorniu-Hernández, E.; Boese, A.-D.; Kusalik, P.-G. *Can. J. Chem.* **2013**, *91*, 544–551.
- (10) Yamaguchi, M. *J. Phys. Chem. A* **2013**, *115*, 14620.
- (11) Asmus, K. D. *Acc. Chem. Res.* **1979**, *12*, 436.
- (12) Göbl, M.; Bonifaičić, M.; Asmus, K. D. *J. Am. Chem. Soc.* **1984**, *106*, 5984.
- (13) Chaudhri, S. A.; Mohan, H.; Anklaam, E.; Asmus, K.-D. *J. Chem. Soc., Perkin Trans. 2* **1996**, 383–390.
- (14) Bobrowski, K.; Pogocki, D.; Schoneich, C. *J. Phys. Chem. A* **1998**, *102*, 10512.
- (15) Kishore, K.; Anklaam, E.; Aced, E. A.; Asmus, K. D. *J. Phys. Chem. A* **2000**, *104*, 9646.
- (16) Asmus, K. D. *Nukleonika* **2000**, *45*, 3.
- (17) Wakamiya, A.; Nishinaga, T.; Komatsu, K. *J. Am. Chem. Soc.* **2002**, *124*, 15038.
- (18) de Visser, S. P.; de Koning, L. J.; Nibbering, N. M. M. *J. Am. Chem. Soc.* **1998**, *120*, 1517.
- (19) de Visser, S. P.; Bickelhaupt, F. M.; de Koning, L. J.; Nibbering, N. M. M. *Int. J. Mass Spectrom.* **1998**, *179–180*, 43.
- (20) Nichols, L. S.; Illies, A. J. *J. Am. Chem. Soc.* **1999**, *121*, 9176.
- (21) King, J. E.; Illies, A. J. *J. Phys. Chem. A* **2004**, *108*, 3581.
- (22) Abu-Raqabah, A.; Symons, M. C. R. *J. Chem. Soc., Faraday Trans. 1990*, *86*, 3293.
- (23) Symons, M. C. R.; Bowman, R. J. *J. Chem. Soc., Perkin Trans. 2* **1990**, 975.
- (24) Rai, U. S.; Symons, M. C. R.; Wyatt, J. L.; Bowman, R. J. *J. Chem. Soc., Faraday Trans. 1993*, *89*, 1199.
- (25) Sevilla, M. D.; Summerfield, S.; Eliezer, I.; Rak, J.; Symons, M. C. R. *J. Phys. Chem. A* **1997**, *101*, 2910.
- (26) Chateaneuf, J. E. *Chem. Commun.* **1998**, *19*, 2099–2100.
- (27) Gauduel, Y.; Launay, T.; Hallou, A. *J. Phys. Chem. A* **2002**, *106*, 1727.
- (28) Balkowski, G.; Szemik-Hojniak, A.; van Stokkum, I. H. M.; Zhang, H.; Buma, W. J. *J. Phys. Chem. A* **2005**, *109*, 3535.

- (29) Scaiano, J. C.; Garca, S.; García, H. *Tetrahedron Lett.* **1997**, *38*, 5929.
- (30) Lakkaraju, P. S.; Shen, K.; Roth, H. D.; García, H. *J. Phys. Chem. A* **1999**, *103*, 7381.
- (31) Sono, M.; Roach, M. P.; Coulter, E. D.; Dawson, J. H. *Chem. Rev.* **1996**, *96*, 2841.
- (32) Shaik, S.; Filatov, M.; Schröder, D.; Schwarz, H. *Chem. - Eur. J.* **1998**, *4*, 193.
- (33) Ogliaro, F.; Harris, N.; Cohen, S.; Filatov, M.; de Visser, S. P.; Shaik, S. *J. Am. Chem. Soc.* **2000**, *122*, 8977.
- (34) Gill, P. M. W.; Radom, L. *J. Am. Chem. Soc.* **1988**, *110*, 4931.
- (35) Do, H.; Besley, N. A. *Phys. Chem. Chem. Phys.* **2013**, *15*, 16214–16219 and references therein..
- (36) Ji, L. F.; Li, A. Y.; Li, Z. Z. *Chem. Phys. Lett.* **2015**, *619*, 115 and references therein..
- (37) Codorniu-Hernández, E.; Kusalik, P.-G. *J. Chem. Theory Comput.* **2011**, *7*, 3725–3732.
- (38) Codorniu-Hernández, E.; Kusalik, P.-G. *J. Am. Chem. Soc.* **2012**, *134*, 532–538.
- (39) Codorniu-Hernandez, E.; Kusalik, P.-G. *Phys. Chem. Chem. Phys.* **2012**, *14*, 11639–11650.
- (40) Codorniu-Hernandez, E.; Hall, K.-Wm.; Ziemianowicz, D.; Carpendale, S.; Kusalik, P.-G. *Phys. Chem. Chem. Phys.* **2014**, *16*, 26094–26102.
- (41) Isaksen, I. S. A.; Dalsøren, S.-B. *Science* **2011**, *331*, 38.
- (42) Trachootham, D.; Alexandre, J.; Huang, P. *Nat. Rev. Drug Discovery* **2009**, *8*, 579–591.
- (43) Valko, M.; Rhodes, C.-J.; Moncol, J.; Izakovic, M.; Mazur, M. *Chem.-Biol. Interact.* **2006**, *160*, 1–40.
- (44) Giorgio, M.; Trinei, M.; Migliaccio, E.; Pelicci, P.-G. *Nat. Rev. Mol. Cell Biol.* **2007**, *8*, 722.
- (45) Martin, G. M.; Austad, S.-N.; Johnson, T.-E. *Nat. Genet.* **1996**, *13*, 25–34.
- (46) Reiter, R.-J.; Melchiorri, D.; Sewerynek, E.; et al. *J. Pineal Res.* **1995**, *18*, 1–11.
- (47) Pelicano, H.; Carney, D.; Huang, P. *Drug Resist. Updates* **2004**, *7*, 97–110.
- (48) Yang, Y.; Bazhin, A.-V.; Werner, J.; Karakhanova, S. *Int. Rev. Immunol.* **2013**, *32*, 249–270.
- (49) Melamede, R. *Mutat. Res.* **1988**, *195*, 215.
- (50) Chipman, D. M. *J. Phys. Chem. A* **2008**, *112*, 13372.
- (51) Vassilev, P.; Louwerse, M.-J.; Baerends, E.-J. *J. Phys. Chem. B* **2005**, *109*, 23605–23610.
- (52) Khalack, J. M.; Lyubartsev, A.-P. *J. Phys. Chem. A* **2005**, *109*, 378.
- (53) VandeVondele, J.; Sprik, M. *Phys. Chem. Chem. Phys.* **2005**, *7*, 1363.
- (54) Alam, M. S.; Janata, E. *Chem. Phys. Lett.* **2006**, *417*, 363.
- (55) Czapski, G.; Bielski, B. H. *Radiat. Phys. Chem.* **1993**, *41*, 503.
- (56) Hill, J. G.; Bucher, G. *J. Phys. Chem. A* **2014**, *118*, 2332–2343.
- (57) Ge, Y.; Olsen, K.; Kaiser, R. I.; Head, J. D. *AIP Conf. Proc.* **2005**, *855*, 253–259.
- (58) Li, J.; Guo, H. *J. Chem. Phys.* **2013**, *138*, 194304.
- (59) Nguyen, T. L.; Stanton, J. F. *J. Phys. Chem. A* **2013**, *117*, 2678–2686.
- (60) Altinay, G.; Macdonald, R.-G. *J. Phys. Chem. A* **2014**, *118*, 38–54.
- (61) Sangwan, M.; Chesnokov, E.-N.; Krasnoperov, L.-N. *J. Phys. Chem. A* **2012**, *116*, 6282–6294.
- (62) Sun, H.; Li, Z. *Chem. Phys. Lett.* **2004**, *399*, 33.
- (63) Allen, A.-O. *Radiat. Res., Suppl.* **1964**, *4*, 54.
- (64) Anbar, M. Water and aqueous solutions. In *Fundamental Processes in Radiation Chemistry*; Ausloos, P., Ed.; Interscience Publishers: New York, 1968; Chapter 10, p 651.
- (65) Bjergbakke, E.; Hart, E. *J. Radiat. Res.* **1971**, *45*, 261.
- (66) Car, R.; Parrinello, M. *Phys. Rev. Lett.* **1985**, *55*, 2471–2474.
- (67) CPMD; IBM Corporation and Max Planck Insitute, Stuttgart.
- (68) Boese, A.-D.; Doltsinis, N.-L.; Handy, N.-C.; Sprik, M. *J. Chem. Phys.* **2000**, *112*, 1670–1678.
- (69) Troullier, N.; Martins, J.-L. *Phys. Rev. B: Condens. Matter Mater. Phys.* **1991**, *43*, 1993–2006.
- (70) Martyna, G.-J.; Klein, M.-L.; Tuckerman, M. *J. Chem. Phys.* **1992**, *97*, 2635.
- (71) Petrenko, V. F.; Whitworth, R.-W. *Physics of Ice*; Oxford University Press Inc, New York, 2002.
- (72) Gunter, T. E. *J. Chem. Phys.* **1967**, *46*, 3818.
- (73) Ghormley, J. A.; Hochanadel, C. J. *J. Phys. Chem.* **1971**, *75*, 40.
- (74) Box, H. C.; Budzinski, E.-E.; Lilga, K.-T.; Freund, H.-G. *J. Chem. Phys.* **1970**, *53*, 1059.
- (75) Stanton, J. F.; Gauss, J.; Harding, M. E.; Szalay, P. G.; et al. CFOUR. <http://www.cfour.de>.
- (76) Werner, H.-J.; Knowles, P. J.; Knizia, G.; Manby, F. R.; Schütz, M.; Celani, P.; Korona, T.; Lindh, R.; Mitrushenkov, A.; Rauhut, G.; Shamasundar, K. R.; Adler, T. B.; Amos, R. D.; Bernhardsson, A.; Berning, A.; Cooper, D. L.; Deegan, M. J. O.; Dobbyn, A. J.; Eckert, F.; Goll, E.; Hampel, C.; Hesselmann, A.; Hetzer, G.; Hrenar, T.; Jansen, G.; Köppl, C.; Liu, Y.; Lloyd, A. W.; Mata, R. A.; May, A. J.; McNicholas, S. J.; Meyer, W.; Mura, M. E.; Nicklaß, A.; O'Neill, D. P.; Palmieri, P.; Peng, D.; Pflüger, K.; Pitzer, R.; Reiher, M.; Shiozaki, T.; Stoll, H.; Stone, A. J.; Tarroni, R.; Thorsteinsson, T.; Wang, M. MOLPRO; University College Cardiff Consultants Limited: Cardiff, UK. <http://www.molpro.net>.
- (77) Sprik, M.; Ciccotti, G. *J. Chem. Phys.* **1998**, *109*, 7737–7745.
- (78) Hall, K. Wm.; Codorniu-Hernández, E.; Kusalik, P. G.; Carpendale, S. ERICAs: Enabling Insights into *ab initio* Molecular Dynamics Simulations, IEEE Pacific Visualization Symposium 2015, Hangzhou, China, April 14–17, 2015; IEEE: 2015; 105–109.
- (79) Adriaanse, C.; Sulpizi, M.; VandeVondele, J.; Sprik, M. *J. Am. Chem. Soc.* **2009**, *131*, 6046–6047.
- (80) Korang, J.; Emahi, I.; Grither, W. R.; Baumann, S. M.; Baum, D. A.; McCulla, R. D. *RSC Adv.* **2013**, *3*, 12390–12397.